MIT Open Access Articles

Laser#Irradiated Holey Graphene#Supported Single#Atom Catalyst towards Hydrogen Evolution and Oxygen Reduction

Massachusetts Institute of Technology

Laser-irradiated holey graphene-supported single-atom catalyst towards hydrogen evolution and oxygen reduction

Kishwar Khan, Tangchao Liu, Muhammad Arif, Xingxu Yan, Md Delowar Hossain, Faisal Rehman, Sheng Zhou, Jing Yang,* Chengjun Sun, Sang-Hoon Bae, Jeehwan Kim, Khalil Amine,* Xiaoqing Pan,* Zhengtang Luo*

Dr. K. Khan, Dr. MD. Hossain, F. Rehman, Prof. Z. Luo
Department of Chemical and Biological Engineering, The Hong Kong University of Science and Technology, Clear Water Bay,
Kowloon 999077, Hong Kong
Email: keztluo@ust.hk (Prof. Z. Luo)

Dr. T. Liu, Prof. K. Amine
Chemical Sciences and Engineering Division, Argonne National Laboratory, 9700 Cass Ave, Lemont, IL 60439, USA

Dr. C. Sun
X-ray Science Division, Argonne National Laboratory,
Lemont, IL 60439, USA

Prof. K. Amine
Chemical Sciences and Engineering Division, Argonne National Laboratory, 9700 Cass Ave, Lemont, IL 60439, USA
Materials Science and Engineering, Stanford University,
Stanford, CA 94305, USA
Institute for Research & Medical Consultations (IRMC), Imam Abdulrahman Bin Faisal University (IAU), Dammam, Saudi Arabia
Email: amine@anl.gov (Prof. K. Amine)

Dr. Muhammad Arif
Institute of Advanced Synthesis (IAS), School of Chemistry and Chemical Engineering, Northwestern Polytechnical University (NPU),
Xi'an 710072, China

Dr. X. Yan, Prof. X. Pan
Department of Materials Science and Engineering, University of California,
Irvine,
CA 92697, USA

Prof. X. Pan
Irvine Materials Research Institute, University of California, Irvine,
Irvine, CA 92697, USA
Department of Physics and Astronomy, University of California, Irvine,

Irvine, CA 92697, USA
Email: xiaoqinp@uci.edu (Prof. X. Pan)

S. Zhou, Prof. J. Yang
Institute of New-Energy Materials, Key Laboratory of Advanced Ceramics and Machining
Technology of Ministry of Education, School of Materials Science and Engineering, Tianjin
University,
Tianjin 300072, China
Email: yang_jing@tju.edu.cn (Prof. J. Yang)

Prof. S.-H. Bae
Department of Mechanical Engineering and Materials Science,
Washington University in Saint Louis,
MO 63130, USA
Institute of Materials Science and Engineering,
Washington University in Saint Louis,
MO 63130, USA
Department of Mechanical Engineering, Massachusetts Institute of Technology,
Cambridge, MA 02139, USA

Prof. S.-H. Bae, Prof. J. Kim
Department of Mechanical Engineering, Massachusetts Institute of Technology,
Cambridge, MA 02139, USA

Keywords

Single-atom catalysts (SAC) can boost intrinsic catalytic activity of hydrogen evolution reaction (HER) and oxygen reduction reaction (ORR). However, the challenge remains due to the complex synthesis process and insufficient stability. A sustainable approach is applied to synthesising SACs through laser irradiation (LI) and gaining mesoporous graphene oxide (MGO). The surface dangling bonds of nitrogen-doped mesoporous graphene oxide (NMGO) extract metal atoms species from Co or Fe metal foams and convert them to SAC via an appropriate synthesis approach. Notably, Co-NMGO electrocatalyst requires low potentials of 146 mV to convey a current density of 10 mA cm^{-2} towards HER. Similarly, Fe-NMGO electrocatalyst offered onset of 0.79 V towards ORR in acidic solution. The individual metal atoms are confirmed via aberration-corrected scanning transmission electron microscopy (AC-STEM), and X-ray absorption near edge structure (XANES) and extended X-ray absorption fine structure (EXAFS). Density functional theory (DFT) calculations by applying the grand

canonical potential kinetics (GCP-K) model revealed that Co-NMGO shows the optimum free reaction energy of -0.17 eV at -0.1 V for HER, and Fe-NMGO has less limiting potential than that of Co-NMGO for ORR case. This work opens a new approach towards the synthesis of SAC and its mechanistic understandings.

Introduction

The current fossil fuel depletion is a massive threat to the environment and energy sustainability[1] and urges us to explore alternative sustainable energy sources.[2] Since 1836, the catalysts research has been explored to take its present shape after Berzelius coined it.[3] To date, electrolysis widely transforms chemicals for practical energy production, storage, and remediation of environmental dents.[4] The selectivity and stability of catalysts are two main factors that drive a reaction in a specific direction and optimize its duration in working conditions. These two factors are majorly dependent on the atomic structure of active sites on the surface, according to the Taylor formulations established in 1925.[5] Catalysts, based on nanomaterials, offer exciting prospects towards present sustainability challenges. The porous structure is considered a successful tactic to tune the surface like area and active sites of the supporting matrix, including nanocarbons.[6] More specifically, mesopores significantly increase the surface area and act as reservoirs for electrolytes, minimizing ion diffusion length.[7] The pores structure contributes to constructing a rational interconnected network[8] that could facilitate ionic transportation through diffusion.[9] The large surface area and improved ion diffusions capabilities of supporting substrates lead to high charging/discharging rates in energy applications.[10] However, pore engineering has rarely been studied to generate efficient supporting materials in electrocatalysis, leading to stabilizing transition metal SAC at the atomic scale. A set of emerging strategies was used to examine sophisticated synthesis methods of catalyst, linked to catalyst's efficiency factors in lowering onset potential and extending their lifetime.[4]

Heterogeneous SAC is referred to as one of the emerging candidates in catalysis due to maximum atomic utilization and specific electronic structures, which greatly enhance performance compared with nano or sub-nanometer counterparts.[11],[12] In recent years, several bottom-up methods are used to synthesize the SAC. However, multistep processes are usually used and are not sustainable due to the enormous waste of metal precursors.[13],[14],[15],[16] In the bottom-up approach, researchers typically use very high temperatures for metal ions reduction

before making a definite structure with SAC sites set with vacancies, which could upturn materials synthesis cost and the highest consumption of energy.[17],[18] Similarly, a top-down approach is usually used to convert metal nanoparticles into SAC; however, high-temperature treatments demolish the support structure, which affects the supporting material's conductivity and lead to a drop in catalytic performance.[19] It is urgent to develop a sustainable synthesis approach that could be environmentally friendly and; cost-effective in ambient conditions to convert bulk metals species to SAC.

Herein, we report the low-intensity pulse laser irradiation technique to synthesis a rich porous graphene oxide support to increase its surface dangling bonds.[20] This technique can precisely tune the in-plane porous structure of graphene oxide (GO) via tuning laser beam energy or laser irradiation time.[21] We applied the concept of the dangling bond of nanocarbons to extract metal species from their bulk metal counterparts at the ambient condition to convert them to SAC directly.[22] Dangling bonds are formed between bulk metal species and reactive non-metal atoms (mainly N or O) because of bulgy geometry configuration on the surface of NMGO support with details listed in the Supplementary Information (SI). We used STEM analysis to confirm the desired morphology, SAC appearances, and its local surroundings. DFT is applied through the grand canonical potential kinetics (GCP-K) model[23],[24] to understand the mechanistic linked to HER and ORR free energy calculation concerning various applied potentials, and we conclude that Co-NMGO shows the superior performance for HER. In contrast, Fe-NMGO has the superior catalytic activity for ORR.
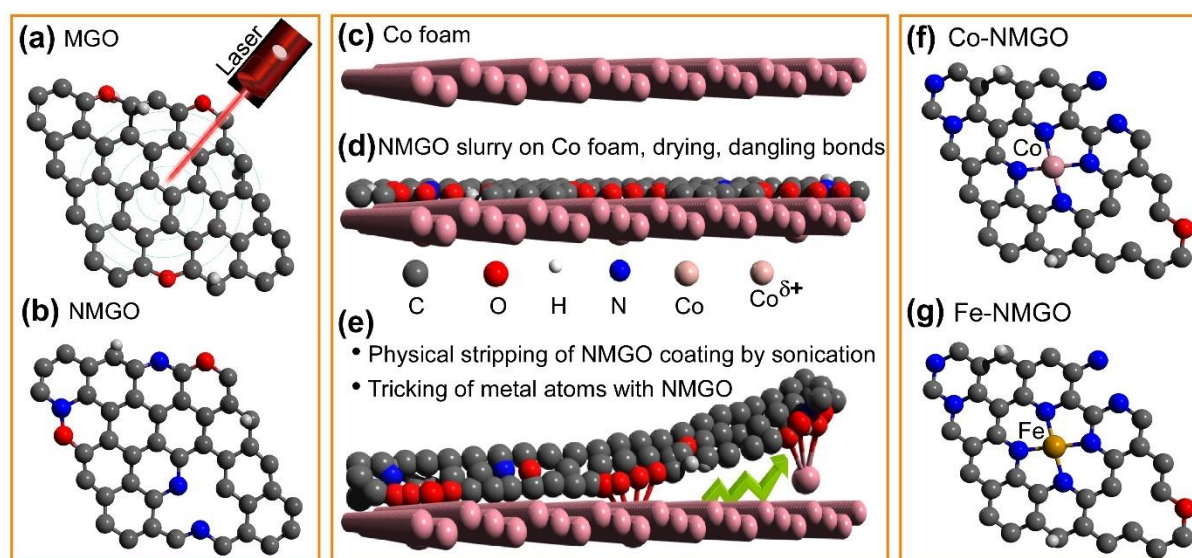

Figure 1. Schematics of laser irradiation on graphene oxide (GO) to fabricate the porous structure. (a) Mesoporous graphene oxide (MGO) was obtained via the pulse laser irradiation process. (b) A hydrothermal process with NH_4HCO_3 is followed to get the nitrogen-doped laser irradiated graphene oxide (NMGO). (c) Metal foam is used as a template. (d) NMGO slurry is

coated on metal foam. (e) Metal single-atom catalyst (SAC) supported on NMGO is obtained by stripping the carbon film. Here we utilized the dangling bonding on nanocarbons to strip the NMGO from metal. (f) Scheme of Co-NMGO SAC catalyst and (g) Fe-NMGO SAC catalyst.

Figure 1 illustrates the material synthesis scheme via the laser irradiation process. GO was used as a starting material to form a porous structure. First, pure GO (5 mg/mL) was diluted with ethanol (3:7) and sonicated at room temperature for 30 min to obtain a uniform solution. The diluted solution was directly irradiated for 30 min with unfocused Nd:YAG pulsed nanosecond laser (1064 nm, 15 Hz, 7 ns) with laser power of 270 mJ in an ice bath to achieve the rich pores structure of nanocarbons as shown in **Figure 1a** and called it MGO. The materials porous structure was verified by Brunauer–Emmett–Teller (BET) analysis, as shown in Figure S1. The considerable in-plane mesopore is introduced in nanocarbon sheets after treating with laser irradiated process.[21] Before the laser irradiation process, abundant micropores is visible in GO nanocarbon support, as shown in Figure S1a; after the laser-irradiated process, the pore radius expands from micropores to mesopores shown in Figure S1b for the case of the MGO sample. It proved that maximum pores are in the range of 45 Å in MGO; such mesopores facilitate the relative concentration of pyridinic N/pyrrolic N during the hydrothermal process for doping nitrogen hybrids with Co, or Fe, abundant mesopores are noticeable, as shown in Figure S1c-e. In **Figure 1b**, the MGO was mixed with N precursor to getting the NMGO via hydrothermal method. The mesopores structure of nanocarbons is generated by periodic irradiation via an unfocused laser irradiated process. The NMGO sample element was checked by STEM-EDS analysis, as shown in Figure S2. It shows a uniform distribution of nitrogen atoms on a carbon support. We applied the fundamental concept of nanocarbon's dangling bonds to extract metal species from bulk counterparts with NMGO support via NMGO surface functional groups' bulgy geometry configuration. Figure 1c used the clean Co or Fe metal foam and deposited the NMGO slurry dropwise to cover the bulk metal foam, as shown in **Figure 1d**. We dried the NMGO slurry on metal foam overnight in the furnace at 45 ℃ to strengthen surface dangling bonds between the metal surface and reactive non-metal atoms. After completely drying NMGO on Co or Fe foam, we sonicated it in ethanol to extract $M^{\sigma+}$ from bulk counterparts and directly convert it to single metal atoms anchored on the NMGO via dangling bonds associated with N/O.[25] The ultra-fast sonication process takes away the metal species to nanocarbon support via surface dangling bonds via a direct interface between nanocarbons and metal foam. The abundant isolated $M^{\delta+}$ species moved to the NMGO support due to charge transfer between transition metal atoms and nitrogen/oxygen atoms. The transition metal mostly bonds with the N/O bonding phenomenon confirmed via XPS analysis

is shown in Figure S3. In **Figure 1e**, the sonication process was applied for 3 hours to extract metal species with NMGO support. The positive metal species ($Co^{\delta+}$ or $Fe^{\delta+}$) takes away with surface nitrogen/oxygen bonds to make Co-N/O or Fe-N/O on NMGO support. After appropriate sintering, the sample was leached to remove the unbonded bulk metal species to get CoN_4 and FeN_4 on NMGO support, as shown in **Figures 1f,g**. We called it Co-NMGO and Fe-NMGO single-atom catalyst. The complete synthesis details are listed in the experimental section of SI.
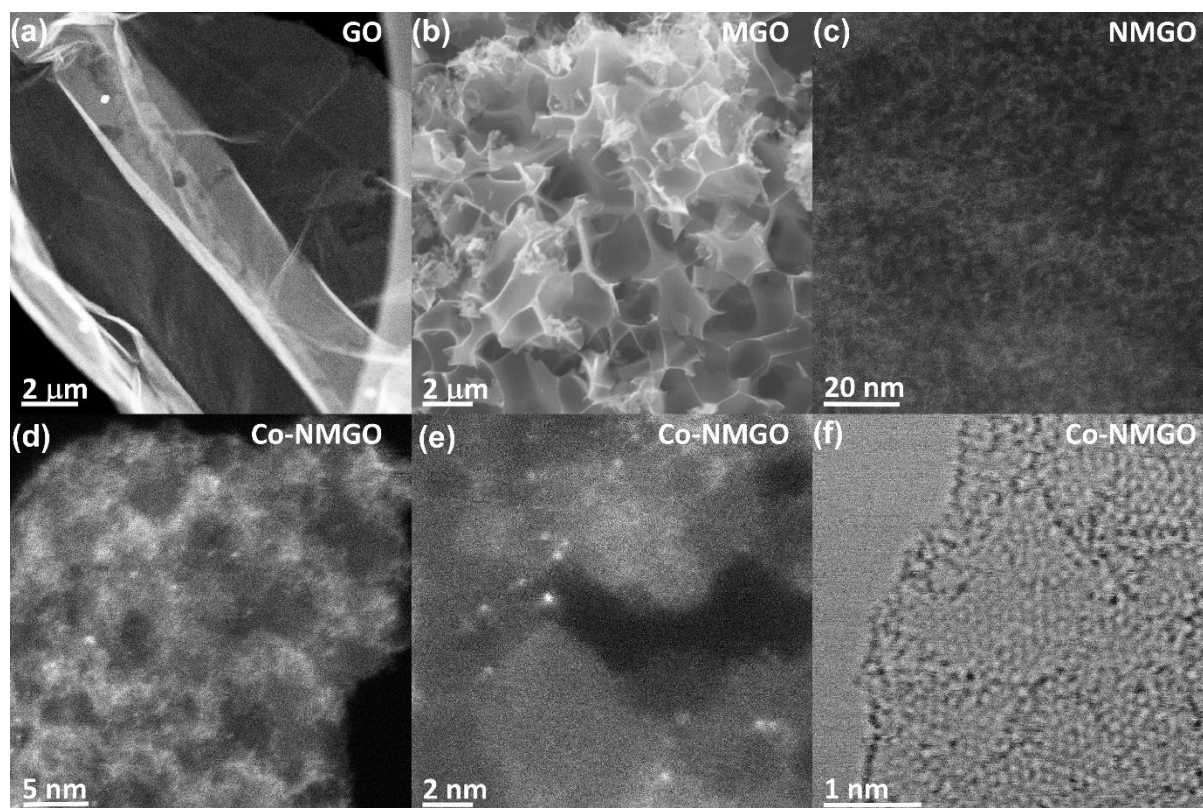

Figure 2. Structure characterization of GO, MGO, NMGO, and Co-NMGO. (a) TEM image of original GO. (b) SEM image of MGO after the laser irradiation, showing the mesoporous 3D architecture. (c) STEM image of NMGO. (d) STEM image of the Co-NMGO sample. (e) Atomic resolution ADF-STEM image of Co-NMGO sample. The bright spots represent heavier metal atoms, manifesting that Co single atoms are atomically dispersed on NMGO support. (f) A bright-field (BF) STEM image of the Co-NMGO sample, showing visible hexagonal rings of graphene lattice.

The surface layered structure morphology of synthesized GO was confirmed by STEM images, as shown in **Figure 2a**. The layered structure is transformed into a rich porous structure via laser irradiation, and its morphology was confirmed via SEM in **Figure 2b** and STEM in **Figure 2c**. SEM confirmed the abundant sharp edges and rich mesopores three-dimensional architecture that could increase catalytic sites on nanocarbon support.[26] Literature suggests that rich mesoporous nanocarbon support have a higher surface area and improves metal loading.[27],[28] It is reported that micropores in nanocarbon matrix are not very supportive

towards mass transportation in terms of high current density.[29] Other reports suggest that the metal SAC case's acid leaching process opens maximum pores during the synthesis process to enlarge the surface area. Reports[27],[28] evidenced that ordered mesopores are majorly hosting metal-doped (MNx) active sites for catalytic applications.

X-ray photoelectron spectroscopy (XPS) analyses the elements and their chemical states of all synthesized samples are analyzed by X-ray photoelectron spectroscopy (XPS). Figure S3 shows that the N peak is visible in all the samples, which confirms N is implanting nanocarbon. We further showed Co, O, N and C in the Co-NMGO sample, and Fe, C, O and N's coexistence is visible for the Fe-NMGO sample shown in Figure S3a. The XPS elemental quantitative compositions of the samples are listed in Table-S1, which shows a good agreement with inductively coupled plasma-mass spectrometry (ICP-MS) measurements Table-S2. No other prominent peak is visible in each sample, indicating the high purity of our applied synthetic approach and fair short-time acid leaching process to remove extra unbounded metal residue contamination.[30] The deconvoluted high-resolution spectra of the NMGO sample is given in Figure S3b. It shows well fitted four individual peaks, including oxidized N, pyridinic-N, pyrrolic-N and graphitic-N.[29, 31] It has been reported that pyridinic N content promotes synthesized catalyst's catalytic activity.[31] Further, rich pyridinic N contents can be served as active sites for anchoring single metal atoms.[32] Figure S3c clarified the N 1s deconvoluted spectra for the Co-NMGO sample. It shown medium level intensity peaks are visible at binding energy (BE) at 398.5 eV (pyridinic N), 399.3 eV (Co-N), 401.2 eV (pyrrolic N), and (graphitic N) at 402.4eV.[33] Similarly, the deconvoluted N 1s spectrum for the Fe-NMGO sample, displayed in Figure S3d. The XPS high-resolution characteristic peaks are fitted into four prominent peaks at BE of 398.5 eV (pyridinic-N), 399.3 eV (Fe-N), 401.3 eV (pyrrolic-N), and 402.3 eV (graphitic-N).[34] N 1s spectrum shows dominant pyridinic N and graphitic N peaks, favorable for ORR performance,[35] and serves as anchoring for Co single-atom sites.[32] Visible small BE difference between Fe-N and pyridinic N's peaks is considered as full pyridinic N.[36] Reports also suggested that the (graphitic-N)[37] and (Fe-N)[38] promote ORR's catalytic activity. Overall, the XPS results shown in Figure S3 indicate that the Co 2p and Fe 2p peaks at 781.1 eV and 710.7 eV respectively of Co-NMGO and Fe-NMGO samples' shifted to higher binding energy, possibly due to increased localized pore densities.[21] Moreover, a high-resolution Co 2p scan in Figure S3e showed two medium intensity peaks related to Co 2p$_{3/2}$ and Co 2p$_{1/2}$ intensity level of (2:1 ratio) concerning binding energy (BE) 781.1 eV and 796.2 eV.[39] In the Co 2p spectrum, the BE energy difference between two prominent peaks is 15.1

eV, which reveal core level signals confirmation corresponding to Co(III) ion.[40] The Fe 2p decomposed spectrum showed two medium level intensity peaks corresponding to Fe $2p_{3/2}$ (710.7 eV) and Fe $2p_{1/2}$ (723.1 eV). It showed the partially oxidized Fe species settling Fe-Nx existence, as shown in Figure S3f.[34] Additionally, the X-ray diffraction (XRD) analysis further confirmed the SAC characteristics[33] of our synthesized Co/Fe-NMGO samples. Our XRD pattern evidences that no other signal is detected associated with metal cluster species in Co-NMGO and Fe-NMGO samples, as shown in Figure S4.

The Co-NMGO and Fe-NMGO samples were further checked by aberration-corrected high-angle annular dark-field STEM (AC HAADF-STEM) imaging to identify the individual Co single atoms dispersed on NMGO support as shown in **Figure 2d,f** and Figure S5a-c. These bright spots are individual heavier atoms, confirming the existence and uniform dispersion of Co single atoms. **Figure 2f** represents the bright-field (BF) image with visible hexagonal rings of graphene lattice at several locations. Similarly, the representative STEM images for the Fe-NMGO sample are shown in Figure S5d-f. The bright spots are heavy atoms uniformly dispersed in NMGO support corresponding to Fe metal species. Overall, STEM representative images shown in Figure S5 justify that the SAC ideally dispersed on NMGO support; without noticeable aggregation in both Co/Fe NMGO samples. It is a fair settlement with an XRD structure illustration given in Figure S4 for Co-NMGO and Fe-NMGO samples. It occupies only one broad peak agreeing to graphitic carbon nature indexed with the (002) plane. No other peak has been detected that corresponding to metal species or their compounds with oxides or nitrides. The absence of metal species is understandable concerning our Co/Fe NMGO samples' atomic catalyst nature. ICP measurements listed in Table-S2 further confirm the small metal quantities in our synthesized SAC. We found Co metal content (0.15 atomic concentration %) and Fe content (0.13 atomic concentration %) in our synthesized Co-NMGO and Fe-NMGO samples.
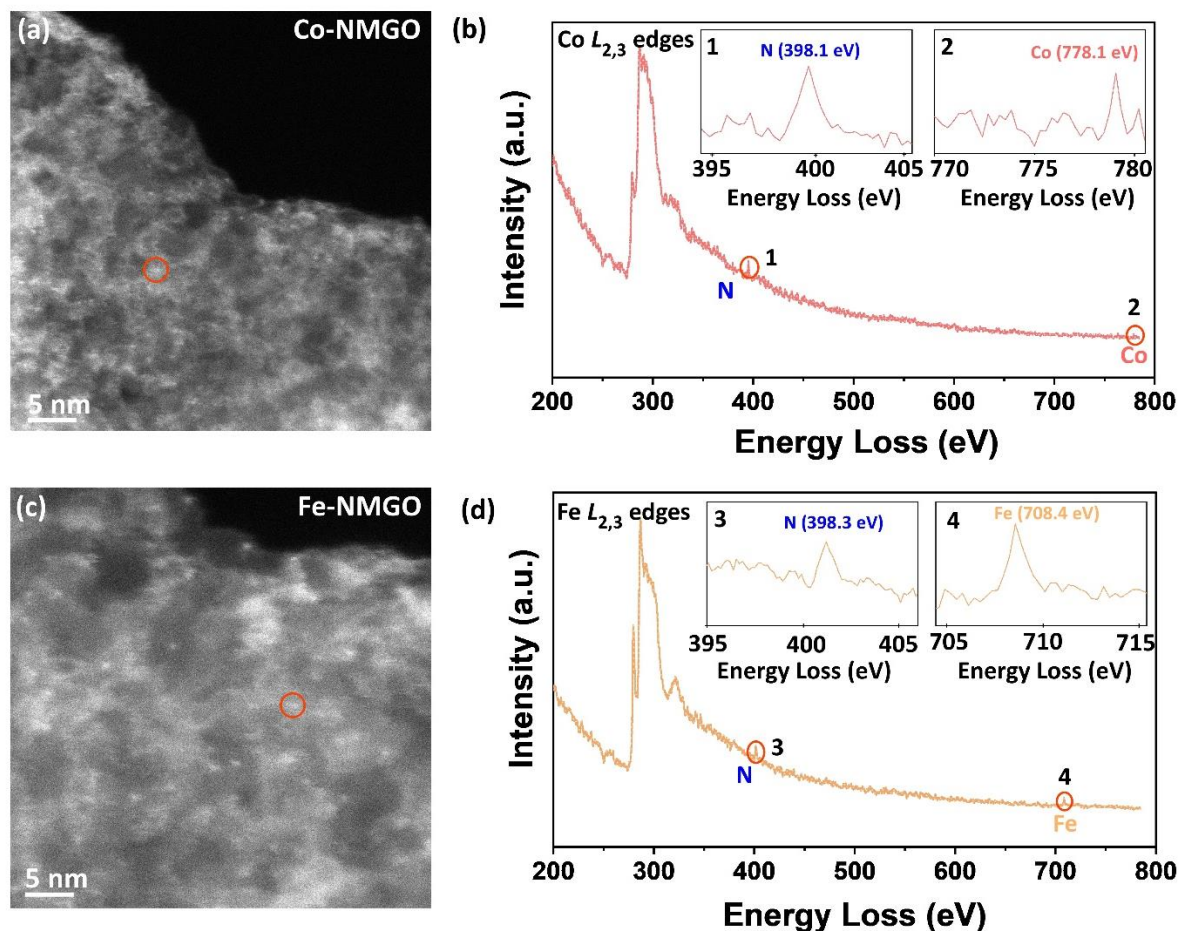
Figure 3. STEM images and EELS characterization of Co-NMGO and Fe-NMGO samples. (a) STEM image of Co-NMGO. (b) EELS analysis from the single atom marked by the red circle in (a). The N and Co are detected on NMGO support at peak positions 1 and 2, respectively. Insets: enlarged EELS spectra of N (#1) and Co (#2) peaks. (c) STEM image of Fe-NMGO. (d) EELS analysis from the single atom marked by the red circle in (c). The N and Fe are detected on NMGO support at peak positions 3 and 4, respectively. In inset: enlarged EELS spectra of N (#3) and Fe (#4) peaks.

The electron energy loss spectroscopy (EELS) analysis further confirmed the brighter atoms are single atom Co and Fe in corresponding Co-NMGO and Fe-NMGO samples, as shown in **Figure 3a,b**. It shows a perfect agreement with XPS analysis. The EDS analysis is given in Figure S6, S7 further confirms the composition of synthesized SAC samples. It shows the ideal dispersion of individual metal atoms on NMGO support.
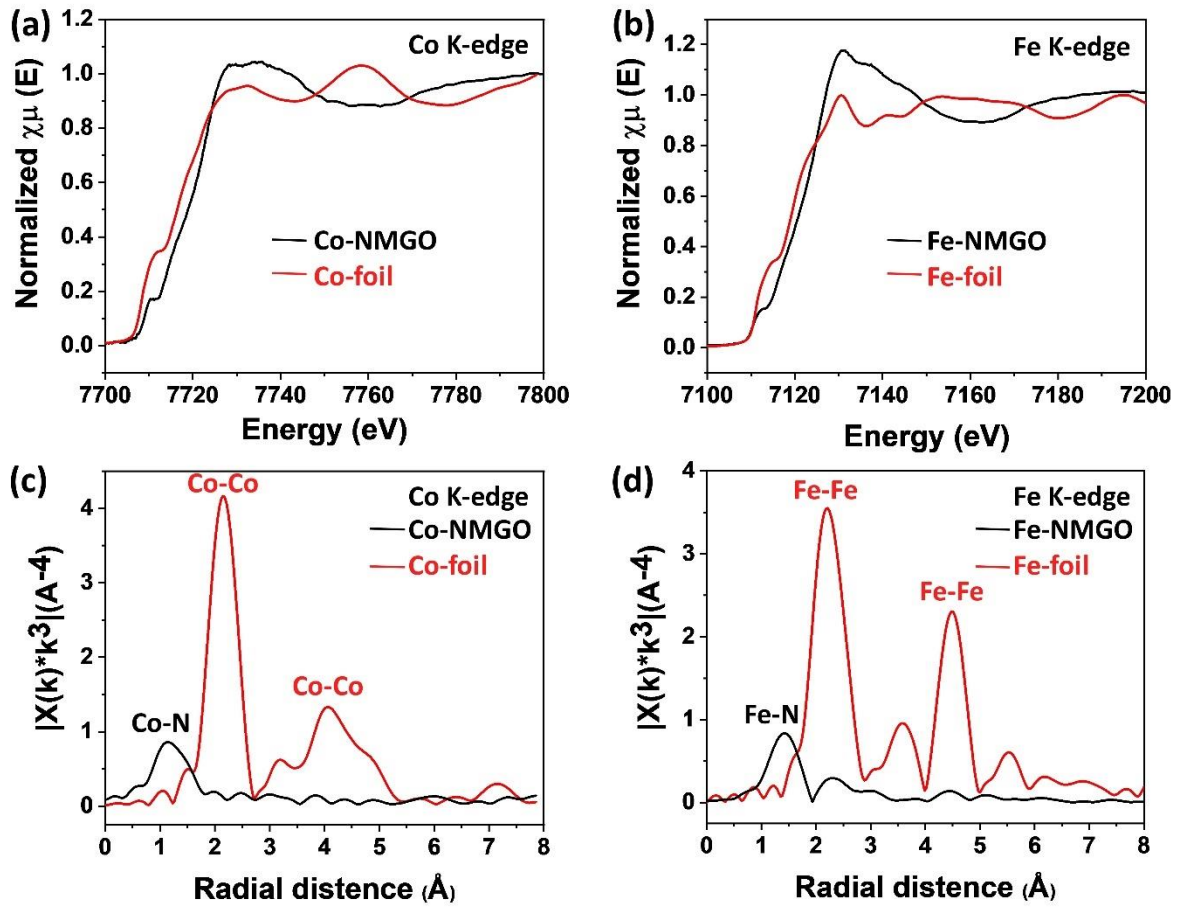
Figure 4. Structure analysis via XANES and EXAFS. (a) Experimental XANES structure of Co K-edge of Co-NMGO sample. (b) Fe K-edge of Fe-NMGO sample. (c) EXAFS spectra of Co-NMGO sample and reference samples. (d) EXAFS spectra of Fe-NMGO sample and reference samples.

The X-ray absorption structure (XAS) with extended X-ray absorption fine structure (EXAFS) is used to confirm Co and Fe's chemical structure and coordination environment. The Co K-edge XANES, as shown in **Figure 4a**, indicates that the absorption edge of Co-NMGO shows a slight right shift compared to Co foil, suggesting that the valence state is a bit higher than 0. The slightly higher valance state of Co should attribute to the coordination between Co and N forming CoN_4.[41] Similarly, **Figure 4b** illustrates a bit higher valance state of Fe in the Fe-NLG due to the formation of FeN_4 coordination.[42] To further confirm the single metal atom's coordination environment, we applied Fourier transform EXAFS measurements for Co-NMGO and Fe-NMGO samples as illustrated in **Figures 4c,d**, respectively. The one prominent peak is visible in both samples corresponding to Co-N (at 1.15 Å) and Fe-N (at 1.4 Å), respectively, which is attributed to isolated Co-N[43] bonds and Fe-N bonds.[44],[45] No prominent peak has been detected related to metal-metal path position. Overall, our

XANES/EXAFS results confirm the excellent dispersion of single metal atoms coordinated with N$_4$ on well-defined NMGO support.
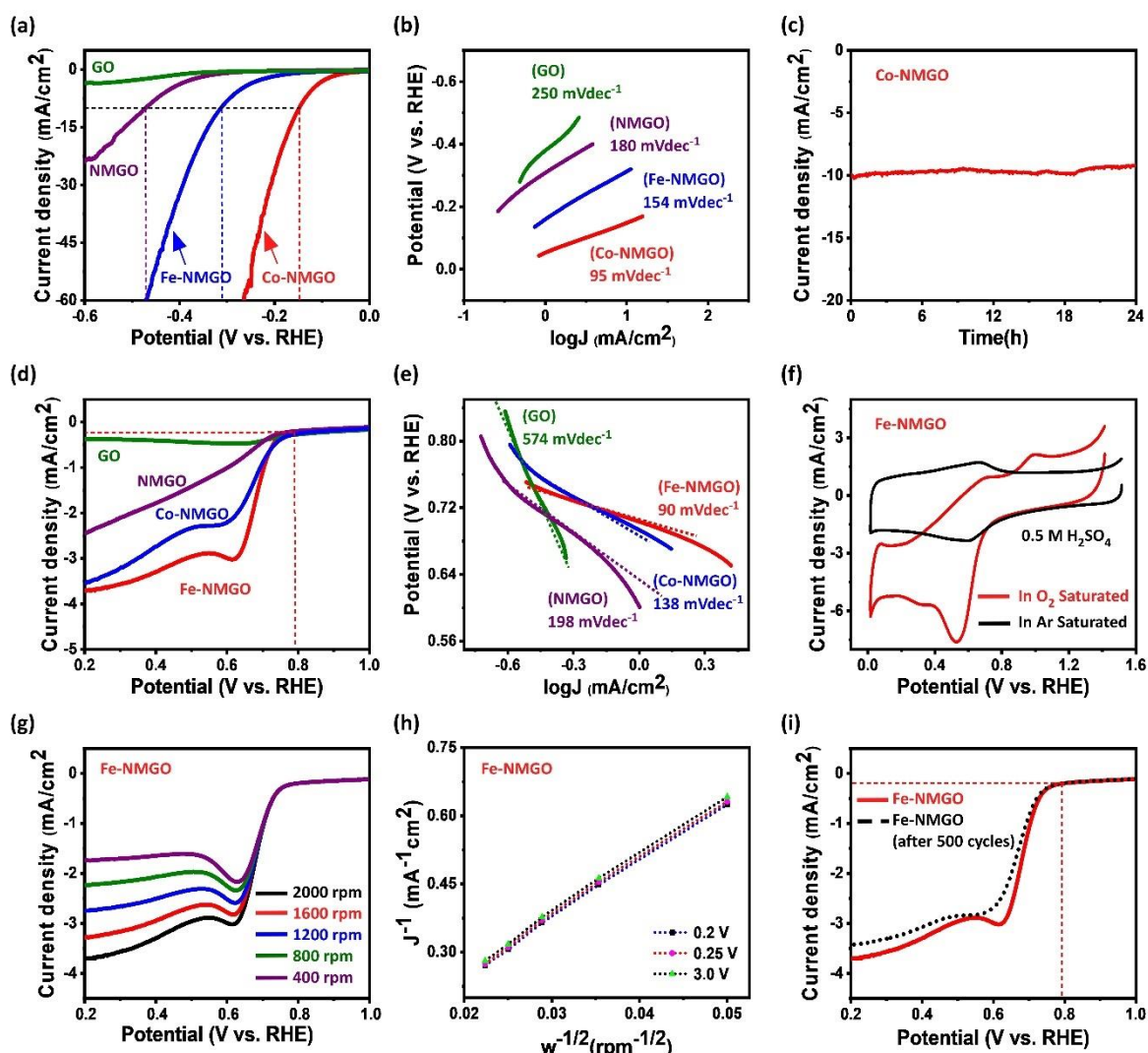

Figure 5. Catalytic performance for HER and ORR. (a) HER LSV plots. (b) Tafel plots. (c) Chronoamperometric measurements of Co-NMGO sample. It showed excellent stability performance for 24 hours. (d) ORR polarization curves. (e) Tafel plots (f) CV curves for Fe-NMGO sample in O$_2$ and air-saturated environment. It illustrates that O$_2$ is rapidly reduced with the Fe-NMGO catalyst. (g) The rotation disk data of the Fe-NMGO sample has numerous rotation speeds to obtain its K-L plot for different potentials, as shown in (h). (i) The stability measurement of the Fe-NMGO sample is measured at 1600 rpm; it showed very stable ORR performance. All catalytic performance was measured in an O$_2$ saturated environment by using 0.5 M H$_2$SO$_4$.

Figure 5 shows the findings of the electrochemical tests of the as-synthesized GO, NMGO, Co-NMGO and Fe-NMGO electrocatalyst. We have scrutinized it by employing a standard three-electrode system. The acidic medium (0.5 M H$_2$SO$_4$) was purged with saturated O$_2$ gas during testing. First, the IR corrected curves were measured from linear sweep voltammetry (LSV) tests. **Figure 5a** shows the HER IR corrected curves for Co-NMGO; it

requires a potential is 146 mV to convey the current density value of 10 mA·cm^{-2}. In contrast, larger potential values of 310 mV, 470 mV and >600 mV are needed to accomplish the identical current density for the Fe-NMGO, NMGO and GO electrocatalyst, respectively. The HER kinetics of the GO, NMGO, Co-NMGO and Fe-NMGO electrocatalyst is also estimated by Tafel slopes obtained from corresponding LSV HER curves shown in **Figure 5b**. However, Co-NMGO delivered the lowest Tafel slope of 95 mV dec^{-1}; this value is smallest among Fe-NMGO (154 mV dec^{-1}), NMGO (180 mV dec^{-1}), and GO (250 mV dec^{-1}), suggesting that the Co-NMGO catalyst has favorable kinetics towards HER. Durability is a significant parameter for assessing the as-synthesized electrocatalyst's electroanalytical activities for practical applications, as shown in **Figure 5c**. Remarkably, Co-NMGO electrocatalyst reveals efficient stability in acidic conditions (0.5 M H$_2$SO$_4$); as recorded in **Figure 5c**, the current density value for Co-NMGO electrocatalyst almost sustained with negligible fluctuations for at least 24 hours is a symbol of excellent stability.

Subsequently, the ORR performance of all synthesized materials is checked, including rotating disk electrode (RDE) tests that have also been done in an acidic medium in 0.5 M H$_2$SO$_4$. The reduction current appeared at +0.79 V vs RHE, corresponding to very low overpotential for the Fe-NMGO sample, as shown in **Figure 5d**. However, for Co-NMGO, NMGO and GO, the onset potential was more negative than Fe-NMGO catalyst. The as-synthesized catalyst is judged through Tafel slope values resulting from corresponding ORR curves shown in **Figure 5e**. Out of all samples, the Fe-NMGO sample delivered the lowest Tafel slope of 90 mV dec^{-1}. This value is comparably lower than Tafel slope values of all catalysts i-e Co-NMGO (138 mV dec^{-1}), NMGO (198 mV dec^{-1}), and GO (250 mV dec^{-1}), suggesting that the Fe-NMGO catalyst has a favorable reaction kinetics towards ORR applications. Cyclic voltammograms (CV) measurements of Fe-NMGO catalyst was accomplished in 0.5 M H$_2$SO$_4$ acidic solution at a scan rate of 50 mV s^{-1} under saturated O$_2$ and Ar, as shown in **Figure 5f**. CV curve of Fe-NMGO under O$_2$ revealed a prominent ORR peak (red line), while the corresponding prominent peak was missing under Ar-saturated electrolyte (black line). The ORR polarization curves of the Fe-NMGO catalyst were checked with various rotation speeds (400−2000 rpm) to obtain Koutecky−Levich (K-L) plots, as shown in **Figures 5g,h**. The electron transfer phenomenon was confirmed for the catalyst via K-L plots. A wide range of applied potentials was examined, and good linearity was achieved, which showed a proficient electron transfer process. Moreover, cycling durability tests were conducted to scrutinize the long-lasting stability of the Fe-NMGO catalyst in O$_2$-saturated

electrolytes shown in **Figure 5i**. After 500 cycles between the potential window of 0 and 1.5 V (vs RHE) at a scan rate of 500 mV s^{-1}, the catalyst retains its onset potential and current density with negligible fluctuations, confirming its impressive durability.
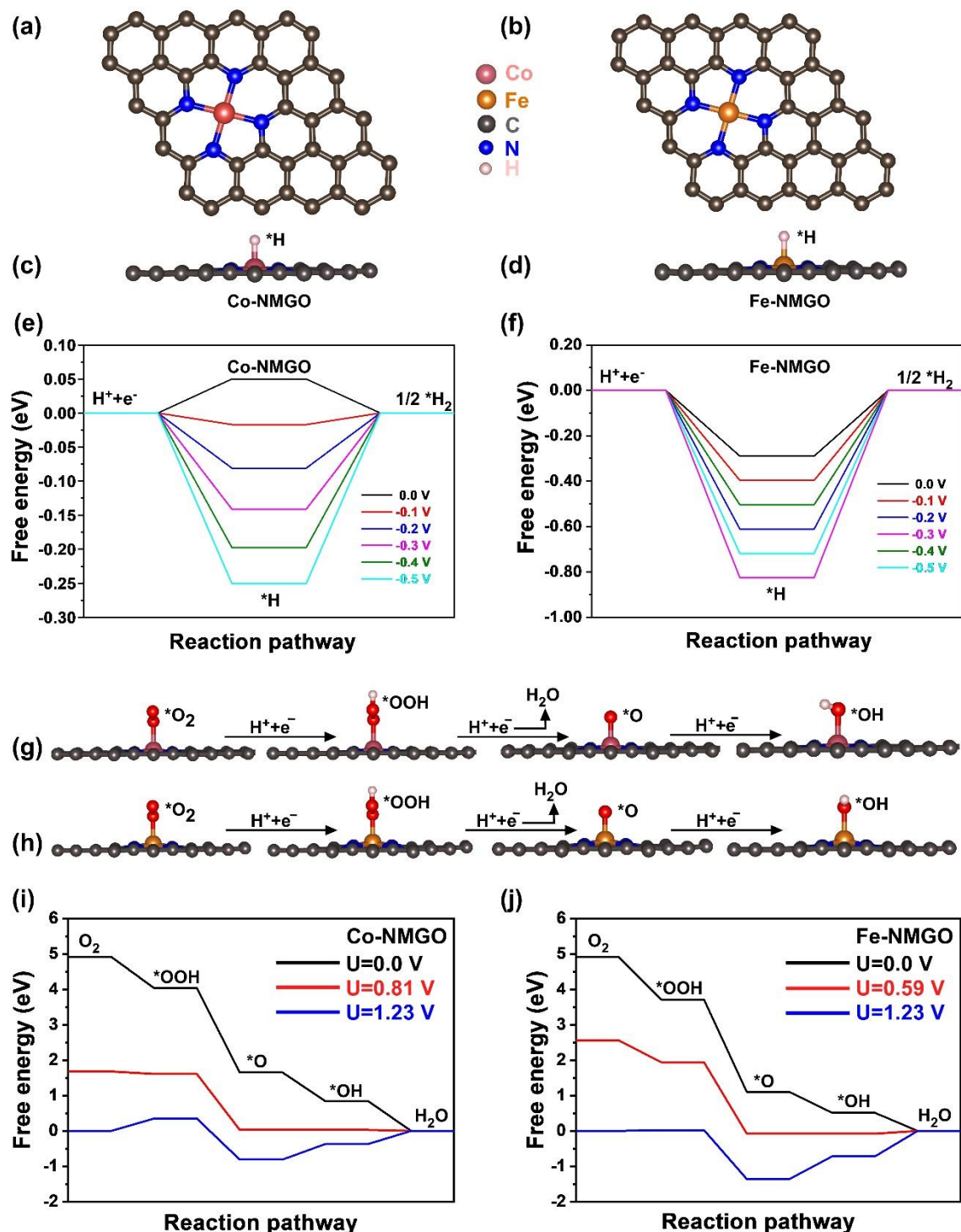

Figure 6. Reaction mechanism and Gibbs free energy calculations for HER and ORR at the constant applied potential. (a-b) The top view of empty substrate and (c-d) side view of H* adsorbed the intermediate state of Co-NMGO, and Fe-NMGO respectively. (e-f) The Gibbs free energy diagram of HER corresponding to Co-NMGO and Fe-NMGO catalyst at various

13

applied potentials. Out of all applied potentials, the Co-NMGO showed the lowest reaction energy of -0.017 eV at applied potential of -0.1 V. (g-h) Literal view of reaction intermediates along the ORR pathway for Co-NMGO and Fe-NMGO, respectively. (i-j) Free energy landscape for ORR in basic media corresponding to Co-NMGO and Fe-NMGO calculated at different applied electrode potentials. For the Co-NMGO case, the ORR has the limiting potential of 0.81 V, while for the Fe-NMGO case, the limiting potential is 0.59 V. (Gray colors balls: carbon, dark blue: nitrogen, red: oxygen, cream: hydrogen, salmon: cobalt, and gold: iron)

DFT calculations were carried out for the mechanistic understanding of the higher catalytic activity. **Figures 6a,b** shows the proposed structural model of Co-NMGO and Fe-NMGO used to predict HER and ORR activity. The configuration of hydrogen adsorption for Co-NMGO and Fe-NMGO catalysts is presented in **Figures 6c,d**. The electrochemical activity for HER and ORR are evaluated by calculating the reaction free energy using a recently developed potential dependent grand canonical potential kinetics (GCP-K) computational method.[46],[24] The Gibbs free energy of hydrogen adsorption (ΔG_{H*}) is a major descriptor of HER activity as the optimal value of ΔG_{H*} is around 0 eV. We have calculated the Volmer step's free energy (as a most critical step for HER) for Co-NMGO and Fe-NMGO at various applied potentials (0.0 to -0.5 eV), as listed in Table-S3. We found that ΔG_{H*} value is 0.05 eV at 0 V vs RHE applied potential decreased to -0.25 eV at -0.5 V vs RHE for Co-NMGO, **Figure 6e**. Similarly, in the Fe-NMGO sample, relatively more negative free energies at corresponding applied potentials indicating strong hydrogen adsorption and making the hydrogen evolution step difficult in **Figure 6f**. Overall, from HER free energy calculations listed in Table-S3, we can conclude that Co-NMGO shows optimum hydrogen adsorption free energy at -0.1 V, which is responsible for the higher catalytic performance than Fe-NMGO catalyst, showing excellent agreement with experimental observations. For ORR mechanistic understanding, we studied the 4e$^-$ pathway for both catalysts, and their corresponding reaction free energies are plotted in **Figures 6g-j**. Initially, the O_2 molecule is adsorbed on the single metal active site as $O_2{}^*$ and protonated to make OOH*. After protonating, OOH* produces water and O*, which is further converted to *OH after being protonated in the next step. Finally, adsorbed OH* is protonated to form H_2O at the final stage. The reaction free energies at different applied potentials using the GCP-K model for ORR pathways on Co-NMGO and Fe-NMGO are shown in **Figures 6i,j**, and corresponding Table-S4. The free energy profile is downhill at zero potential for both cases, where Fe-NMGO shows lower free energy than Co-NMGO at the same conditions. When we applied potential to these systems, the free energy of *O and *OH steps becomes equal at 0.59 V applied potential for Fe-NMGO and 0.81 V for Co-NMGO, respectively, considering downhill energy profile (red line in **Figure 5i,j**). So, in comparison, the limiting

14

potential for Fe-NMGO (0.59 V) is smaller than that of Co-NMGO (0.81 V), which confirms that Co-NMGO at various potentials is uncomplimentary under the applied potential condition. At the same time, Fe-NMGO electrocatalyst shows greater activity under the same electrolytic conditions. This theoretical prediction shows excellent agreement with experimental findings.

In conclusion, laser irradiation was successfully applied to synthesize the rich porous structure of GO. A new synthetic approach based on dangling bonds is applied to trap metal species with NMGO support, followed by appropriate conditions to convert into SAC. Our laser irradiation approach is feasible for various layered structure materials (metal oxide, etc.) to refrain from the defect's density and pore size. The dangling bonds concept provide a facile sustainable route for developing SAC for various important reactions like oxygen evolution reaction (OER), CO_2 reduction reaction (CO_2RR), and nitrogen reduction reaction (NRR). It is a sustainable approach to grab the single metal atoms from their bulk counterpart with the help of entire surface dangling bonds of nanocarbon functional groups. Furthermore, our applied GCP model provides new insights into current electrochemistry research to understand the reaction mechanism deeply. It applies to other critical electrochemical reactions soon.

Author contributions
Dr. K. Khan conceived the project, synthesized the materials, performed the experimental characterizations & wrote the manuscript. Dr. T. Liu, Dr. C. Sun and Prof. K. Amine., performed the XANES/EXAFS experiments at Argonne Photon Source (APS), Argonne National Laboratory (ANL). Dr. M. Arif performed catalytic reactions experiments for all samples. Dr. X. Yan and Prof. X. Pan performed STEM and EELS analysis. Dr. MD. Hossain and F. Rehman performed DFT calculation. S. Zhou, and Prof. J. Yang., use Nd: YAG laser at Tianjin University for sample preparation. Prof. S.-H. Bae and Prof. J. Kim helped in the overall discussion and revision. Overall, Prof. K. Amine and Prof. Z. Luo., supervised the project. All contributed authors discussed and commented on the manuscript.

Conflict of Interests: The authors declare no conflict of interest.

References

[1]   S. Chu, Y. Cui, N. Liu, Nature Materials 2017, 16, 16.
[2]   S. Chu, A. Majumdar, Nature 2012, 488, 294.
[3]   J. Berzelius, Ann. Chim 1836, 61, 146.
[4]   S. Mitchell, R. Qin, N. Zheng, J. Pérez-Ramírez, Nature Nanotechnology 2021, 16, 129.
[5]   H. S. Taylor, Proceedings of the Royal Society of London. Series A, Containing Papers of a Mathematical and Physical Character 1925, 108, 105.
[6]   M. Salanne, B. Rotenberg, K. Naoi, K. Kaneko, P. L. Taberna, C. P. Grey, B. Dunn, P. Simon, Nat. Energy 2016, 1, 16070.
[7]   H. Peng, B. Yao, X. Wei, T. Liu, T. Kou, P. Xiao, Y. Zhang, Y. Li, Advanced Energy Materials 2019, 9, 1803665.
[8]   K. S. W. Sing, Pure and Applied Chemistry 1985, 57, 603.
[9]   M. Salanne, B. Rotenberg, K. Naoi, K. Kaneko, P. L. Taberna, C. P. Grey, B. Dunn, P. Simon, Nature Energy 2016, 1, 16070.
[10]   H. Peng, B. Yao, X. Wei, T. Liu, T. Kou, P. Xiao, Y. Zhang, Y. Li, Adv. Energy Mater. 2019, 9, 1803665.
[11]   J. Gu, C.-S. Hsu, L. Bai, H. M. Chen, X. Hu, Science 2019, 364, 1091; L. Cao, Q. Luo, W. Liu, Y. Lin, X. Liu, Y. Cao, W. Zhang, Y. Wu, J. Yang, T. Yao, S. Wei, Nature Catalysis 2019, 2, 134.
[12]   H. Bao, Y. Qiu, X. Peng, J.-a. Wang, Y. Mi, S. Zhao, X. Liu, Y. Liu, R. Cao, L. Zhuo, J. Ren, J. Sun, J. Luo, X. Sun, Nature Communications 2021, 12, 238.
[13]   J. Lin, A. Wang, B. Qiao, X. Liu, X. Yang, X. Wang, J. Liang, J. Li, J. Liu, T. Zhang, J. Am. Chem. Soc. 2013, 135, 15314.
[14]   L. Lin, W. Zhou, R. Gao, S. Yao, X. Zhang, W. Xu, S. Zheng, Z. Jiang, Q. Yu, Y.-W. Li, C. Shi, X.-D. Wen, D. Ma, Nature 2017, 544, 80.
[15]   H. Yan, H. Cheng, H. Yi, Y. Lin, T. Yao, C. Wang, J. Li, S. Wei, J. Lu, J. Am. Chem. Soc. 2015, 137, 10484.
[16]   L. Cao, W. Liu, Q. Luo, R. Yin, B. Wang, J. Weissenrieder, M. Soldemo, H. Yan, Y. Lin, Z. Sun, C. Ma, W. Zhang, S. Chen, H. Wang, Q. Guan, T. Yao, S. Wei, J. Yang, J. Lu, Nature 2019, 565, 631.
[17]   K. Ding, A. Gulec, A. M. Johnson, N. M. Schweitzer, G. D. Stucky, L. D. Marks, P. C. Stair, Science 2015, 350, 189.
[18]   Z. Zhang, Y. Zhu, H. Asakura, B. Zhang, J. Zhang, M. Zhou, Y. Han, T. Tanaka, A. Wang, T. Zhang, N. Yan, Nat. Commun. 2017, 8, 16100.
[19]   Q. Wang, X. Wang, F. Wan, K. Chen, Z. Niu, J. Chen, Small 2018, 14, 1800280.
[20]   J. Li, R. Cui, Y. Chang, H. Huang, X. Guo, J. Wang, R. Liu, K. Chen, J. Kong, G. Xing, B. Sun, RSC Advances 2020, 10, 36378.
[21]   X.-R. Wang, J.-Y. Liu, Z.-W. Liu, W.-C. Wang, J. Luo, X.-P. Han, X.-W. Du, S.-Z. Qiao, J. Yang, Advanced Materials 2018, 30, 1800005.
[22]   Y. Qu, L. Wang, Z. Li, P. Li, Q. Zhang, Y. Lin, F. Zhou, H. Wang, Z. Yang, Y. Hu, M. Zhu, X. Zhao, X. Han, C. Wang, Q. Xu, L. Gu, J. Luo, L. Zheng, Y. Wu, Advanced Materials 2019, 31, 1904496.
[23]   Y. Huang, R. J. Nielsen, W. A. Goddard, J. Am. Chem. Soc. 2018, 140, 16773.
[24]   M. D. Hossain, Y. Huang, T. H. Yu, W. A. Goddard Iii, Z. Luo, Nature Communications 2020, 11, 2256.
[25]   X. Zhang, S. Zhang, Y. Yang, L. Wang, Z. Mu, H. Zhu, X. Zhu, H. Xing, H. Xia, B. Huang, J. Li, S. Guo, E. Wang, Advanced Materials 2020, 32, 1906905; J.-F. Sun, Q.-Q. Xu, J.-L. Qi, D. Zhou, H.-Y. Zhu, J.-Z. Yin, ACS Sustainable Chemistry & Engineering 2020, 8, 14630.
[26]   H. Wang, X.-B. Li, L. Gao, H.-L. Wu, J. Yang, L. Cai, T.-B. Ma, C.-H. Tung, L.-Z. Wu, G. Yu, Angewandte Chemie International Edition 2018, 57, 192.
[27]   M. Lefèvre, E. Proietti, F. Jaouen, J.-P. Dodelet, Science 2009, 324, 71.

[28]   X. Xie, C. He, B. Li, Y. He, D. A. Cullen, E. C. Wegener, A. J. Kropf, U. Martinez, Y. Cheng, M. H. Engelhard, M. E. Bowden, M. Song, T. Lemmon, X. S. Li, Z. Nie, J. Liu, D. J. Myers, P. Zelenay, G. Wang, G. Wu, V. Ramani, Y. Shao, Nat. Cat. 2020, 3, 1044.

[29]   Y.-L. Wu, X. Li, Y.-S. Wei, Z. Fu, W. Wei, X.-T. Wu, Q.-L. Zhu, Q. Xu, Advanced Materials 2021, n/a, 2006965.

[30]   W. Zhong, Z. Wang, S. Han, L. Deng, J. Yu, Y. Lin, X. Long, M. Gu, S. Yang, Cell Reports Physical Science 2020, 1, 100115.

[31]   Q. Cheng, L. Yang, L. Zou, Z. Zou, C. Chen, Z. Hu, H. Yang, ACS Catalysis 2017, 7, 6864.

[32]   P. Yin, T. Yao, Y. Wu, L. Zheng, Y. Lin, W. Liu, H. Ju, J. Zhu, X. Hong, Z. Deng, G. Zhou, S. Wei, Y. Li, Angewandte Chemie International Edition 2016, 55, 10800.

[33]   C. Zhu, Q. Shi, B. Z. Xu, S. Fu, G. Wan, C. Yang, S. Yao, J. Song, H. Zhou, D. Du, S. P. Beckman, D. Su, Y. Lin, Advanced Energy Materials 2018, 8, 1801956.

[34]   L. Jiao, G. Wan, R. Zhang, H. Zhou, S.-H. Yu, H.-L. Jiang, Angewandte Chemie International Edition 2018, 57, 8525.

[35]   L. Lai, J. R. Potts, D. Zhan, L. Wang, C. K. Poh, C. Tang, H. Gong, Z. Shen, J. Lin, R. S. Ruoff, Energy & Environmental Science 2012, 5, 7936.

[36]   H.-W. Liang, W. Wei, Z.-S. Wu, X. Feng, K. Müllen, Journal of the American Chemical Society 2013, 135, 16002.

[37]   R. Jiang, L. Li, T. Sheng, G. Hu, Y. Chen, L. Wang, Journal of the American Chemical Society 2018, 140, 11594.

[38]   X. Cui, S. Yang, X. Yan, J. Leng, S. Shuang, P. M. Ajayan, Z. Zhang, Advanced Functional Materials 2016, 26, 5708.

[39]   H. Fei, J. Dong, M. J. Arellano-Jiménez, G. Ye, N. Dong Kim, E. L. G. Samuel, Z. Peng, Z. Zhu, F. Qin, J. Bao, M. J. Yacaman, P. M. Ajayan, D. Chen, J. M. Tour, Nature Communications 2015, 6, 8668.

[40]   E. S. Andreiadis, P.-A. Jacques, P. D. Tran, A. Leyris, M. Chavarot-Kerlidou, B. Jousselme, M. Matheron, J. Pécaut, S. Palacin, M. Fontecave, V. Artero, Nature Chemistry 2013, 5, 48.

[41]   X. Wang, Z. Chen, X. Zhao, T. Yao, W. Chen, R. You, C. Zhao, G. Wu, J. Wang, W. Huang, J. Yang, X. Hong, S. Wei, Y. Wu, Y. Li, Angew.Chem. Int. Ed. 2018, 57, 1944; T. Sun, S. Zhao, W. Chen, D. Zhai, J. Dong, Y. Wang, S. Zhang, A. Han, L. Gu, R. Yu, X. Wen, H. Ren, L. Xu, C. Chen, Q. Peng, D. Wang, Y. Li, Proceedings of the National Academy of Sciences 2018, 115, 12692.

[42]   Y. Chen, S. Ji, Y. Wang, J. Dong, W. Chen, Z. Li, R. Shen, L. Zheng, Z. Zhuang, D. Wang, Y. Li, Angewandte Chemie International Edition 2017, 56, 6937.

[43]   H. Fei, J. Dong, M. J. Arellano-Jiménez, G. Ye, N. Dong Kim, E. L. G. Samuel, Z. Peng, Z. Zhu, F. Qin, J. Bao, M. J. Yacaman, P. M. Ajayan, D. Chen, J. M. Tour, Nat. Commun. 2015, 6, 8668.

[44]   L. Yang, D. Cheng, H. Xu, X. Zeng, X. Wan, J. Shui, Z. Xiang, D. Cao, P. Nat. Acad. Sci. 2018, 115, 6626.

[45]   J.-D. Yi, R. Xu, Q. Wu, T. Zhang, K.-T. Zang, J. Luo, Y.-L. Liang, Y.-B. Huang, R. Cao, ACS Energy Letters 2018, 3, 883.

[46]   Y. Huang, R. J. Nielsen, W. A. Goddard, Journal of the American Chemical Society 2018, 140, 16773.